Stabilization of Unprecedented Crystal Phases of Metal Nanomaterials

Kenshi Matsumoto,[1] Ryota Sato,[1] and Toshiharu Teranishi[1,2*]

[1]Institute for Chemical Research, Kyoto University, Gokasho, Uji, Kyoto 611-0011, Japan

[2]Department of Chemistry, Graduate School of Science, Kyoto University, Gokasho, Uji, Kyoto 611-0011, Japan

Abstract

Metal nanomaterials (NMs) have attracted much attention from both scientific and practical perspectives. Because the crystal structure of metal NMs is a crucial factor in determining corresponding physicochemical properties, investigations of unprecedented crystal structures facilitate development of new functions and enhancement of well-known properties. Although an infinite number of crystal structures are geometrically possible, formation of experimentally known crystal structures depends on thermodynamics. Here, we introduce synthetic strategies for new frameworks of mono-metal and alloy NMs as well as unprecedented ordered structures of alloy NMs, reveal the contribution to enhanced catalysis of the hydrogen evolution and oxygen reduction reactions, and provide perspectives on catalytic properties that depend on unique crystal structures.

Crystal structures against thermodynamics in metal nanomaterials

The crystal structure of metal nanomaterials (NMs) is a crucial factor in determining corresponding physical and chemical properties [1-4], indicating that phase control and

investigating new-type crystal structures (not represented by well-known crystal structures) are quite important for developing new functions as well as enhancing well-known properties. For that purpose, NMs are attractive because the phase stability substantially changes with decreasing size—caused by decreasing the **cohesive energy** (see Glossary), melting point, and Debye temperature; and increasing the surface energy (nano-size effect) [5-8]. In recent reports, many **solid–solution alloy** NMs composed of immiscible elements in bulk [1, 2, 9-15], and binary alloy [16-20] as well as mono-metal [4, 21-30] NMs with metastable crystal structures, have been obtained (Box 1). For example, two metallic elements—Ag and Rh—that are not miscible in bulk afford Ag−Rh solid–solution alloy NMs because of the nano-size effect [9]. Similarly, the nano-size effect enabled us to generate *A*3 [hexagonal close-packed (*hcp*)-type solid–solution] Pt–Ni [17] and face-centered cubic (*fcc*)-Ru NMs [4], whereas *A*1 (*fcc*-type solid–solution) Pt–Ni and *hcp* Ru were thermodynamically stable in bulk. These NMs exhibited superior catalytic properties in the hydrogen evolution, ethanol oxidation, oxygen reduction, CO oxidation, NO reduction, and C_3H_6 oxidation reactions compared with representative catalysts such as *fcc*-Pt and *fcc*-Rh [1, 17-19, 29, 31, 32].

However, there are few reports on forming mono-metal and alloy NMs with unprecedented phases containing ordered stacking faults, ordered point defects, or unknown atomic-layer stacking fashions—even though various metastable phases could be stabilized by the nano-size effect [18, 27-29, 32]. Whereas thermodynamically stable phases are generally formed, an infinite number of crystal structures are geometrically possible [33]. In fact, considering all of the crystal structures of recently obtained mono-metals and alloys with metastable phases [1, 2, 4, 9-17, 19-26, 30], atomic arrangements are represented only by changing the constituent elements of well-known crystal

structures such as *fcc*, *hcp*, $L1_0$ (CuAu-type), $L1_1$ (CuPt-type), and $L1_2$ (Cu_3Au-type) phases. Therefore, forming unprecedented crystal structures is quite challenging and is necessary for advancing materials science because the lack of known crystal structures might hinder development of new functions and enhancement of well-known properties. The nano-size effect [18, 27-29, 32], lattice strain [18, 28, 32], particle morphology [29], or an additional third element [34] are prerequisites for stabilizing metastable phases with well-known or unprecedented crystal structures. In this review, we introduce examples of synthesizing mono-metal and alloy NMs with unprecedented crystal structures (ordered stacking faults, ordered point defects, and unique layered structures) (Table 1), and explain the enhanced catalytic activities as a promising application arising from the unprecedented phases.

New frameworks of mono-metal nanomaterials

Ordered stacking faults

Representative close-packed structures such as *fcc* and *hcp* phases are denoted as 3C and 2H, respectively; where C is cubic, H is hexagonal, and the numerical characters are repeating numbers of a close-packed plane such as ABC, ABC,… and AB, AB,…. By this representation, 3C is regarded as the ordered stacking fault of 2H and vice versa. Based on this rule, many new-type crystal structures with a different ordered stacking fault such as ABCB, ABCB,… (4H) and ABCBCB, ABCBCB,… (6H) are considered (Figure 1A) [35]. Although stacking faults are evident in many materials [36-39], the transformation from well-known to new structures with ordered stacking faults are quite rare because introducing ordered stacking faults is thermodynamically unstable.

In 2011, Chakraborty *et al.* calculated the cohesive energies of 3C, 2H, 4H, and 6H

of Ag and Au in accordance with **first-principles calculations**, from which the order of the stability was 3C > 6H > 4H > 2H [35]. In 2011 and 2012, Huang *et al.* synthesized Au nanowires and nanosheets with a 2H crystal structure [26, 40]. These reports indicate that Au NMs with 4H and 6H structures can be synthesized; i.e., 2H is expected to transform into more-stable 4H or 6H structures if one provides appreciate external stimuli, such as a moderate heat and pressure. The first success in forming a 4H structure was achieved by growth from Au nanowires (1.4–2.0 nm) with an 2H structure formed at 58 °C for 4 h to nanoribbons (2.8–5.2, 8.0–20.0, and 15.0–61.0 nm obtained for reaction times of 8, 12, and 16 h, respectively) (Figure 1B–E) [27], arising from the larger cohesive energy of the 4H structure than that of the 2H structure. As a similar phenomenon, an increase in the Ru shell thickness on *fcc*-Pd nanoplates induced a transformation of metastable (*fcc*) to stable phases (*hcp*) of Ru shells because of the larger **bulk energy** of *fcc*-Ru than that of *hcp*-Ru [23, 41]. As an another example, Au nanospheres including three components of 3C, 2H, and 4H structures were synthesized via dealloying of *A*3-Au−Ga [42], indicating that 2H-type Au substructure in *A*3-Au−Ga facilitated the kinetic formation of more stable 4H phase. Because the 4H structure of Au is also an unfavorable phase, 6H or other ordered stacking fault structures of Au could be formed by choosing an appropriate driving force (Box 2).

4H and different ordered stacking fault structures were also fabricated by epitaxial growth of mono-metals (Ag, Rh, Os, Ru, Cu, and Co) and solid–solution alloys (Pt−Cu, Pt−Co, Ag−Pd, Pt−Ag, and Pt−Pd−Ag) on 4H-Au nanoribbons [18, 28, 32, 43, 44]. When using this approach, the lattice mismatch at the interface between the close-packed planes of Au and other metals is an important factor in determining the crystal structures of metals on 4H-Au. Epitaxial growth proceeds at a lattice mismatch of <5% [45], resulting

in the formation of Ag and solid–solution Ag−Pd, Pt−Ag, and Pt−Pd−Ag alloys with a 4H structure on 4H-Au [44]. Surprisingly, even when the lattice mismatch is >5%, 4H Rh, Os, Ru, Cu, Pt−Cu, and Pt−Co nanostructures on 4H Au nanoribbons were also fabricated [18, 43]; which indicates that many mono-metals and alloys have the potential to form the 4H structure. However, a much larger lattice mismatch between Co/Au (~14%) did not afford 4H-Co but instead unique ordered misfit dislocations of 14H-Co nanoribbons ($BCBABA_DCBABCBC_DA$, $BCBABA_DCBABCBC_DA$,…) (Figure 1F–H) [28].

These reports on forming new-type ordered stacking faults indicate that previously synthesized 4H and 14H structures as well as 6H and other ordered stacking faults structures can be synthesized, for many mono-metal and alloy NMs, by choosing an appreciate driving force such as an increase in the particle size, dealloying process, and lattice mismatch. In addition, various metastable mono-metals and alloys with well-known structures except for the Au system could also be synthesized [1, 2, 4, 9-17, 19-25, 30]. This reveals the possibility of a phase transformation from well-known metastable structures to more-stable new-type structures; including 4H, 14H, 6H, and other ordered stacking fault structures.

Ordered point defects

Point defects are an essential feature of mono-metal and alloy NMs, and can facilitate atomic diffusion in NMs, known as the **Kirkendall effect** [46, 47]. Usually, point defects are randomly distributed in NMs in a manner that decreases the Gibbs free energy [48]. Therefore, forming NMs with ordered point defects is challenging, and introducing ordered point defects into well-known mono-metals affords a large number of crystal structure candidates, as evident in binary alloys.

Recently, Zhang *et al*. reported kinetic formation of Rh NMs with a metastable phase (*hcp*) and unfavorable short-range ordered point defects (Figure 2A and G–J) [29]. In accordance with high-resolution transmission electron microscopy (HRTEM), the morphology of *hcp*-type Rh NMs with short-rage ordered point defects consisted of many nanosheets stacked on an atomic level (Figure 2C–F). Such a unique morphology was fabricated via growth of Rh NMs with a small quantity of short and thin nanosheets (10–20, 40–70, 120–180, and 218±31 nm overall size obtained for reaction times of 1, 3, 6, and 14 h, respectively) (Figure 2K); whereas *hcp* phase was formed within 1 h and *hcp*-type structures with short-range ordered point defects were evident after 3, 6, and 14 h. In addition, the thickness of the nanosheets in Rh NMs obtained after a reaction time of 14 h was 3.7±1.1 nm. These experimental results indicate that atomic-level intercalated nanosheets formed after 1 h cause extremely slow Rh atom diffusion in a manner that facilitates further growth in *hcp*-Rh nanosheets (Figure 2L), resulting in insufficient introduction of Rh atoms in Rh nanosheets in a manner that kinetically forms thermodynamically unfavorable crystal structures, or ordered point defects in *hcp*-type Rh. However, annular bright-field scanning TEM (ABF-STEM) indicates insertion of carbon in *hcp*-type Rh with ordered point defects, which is not negligible for elucidating the driving force for forming such unfavorable crystal structures [49]. As another factor for forming ordered point defects in *hcp*-type Rh, the instability of *hcp*-Rh compared with the most stable *fcc*-Rh might be also considered [41]. For clearly elucidating the driving force, more investigations are necessary. This research reveals that an appreciate design of the particle morphology enables kinetics-based fabrication of mono-metal or alloy NMs with ordered point defects.

Unprecedented ordered alloy nanomaterials

An infinite number of crystal structures are geometrically conceivable in **intermetallic binary alloys**, but only thermodynamically stable phases and several metastable phases were formed in previous reports (Box 3) [50-54]. In the case of layer-structured ordered binary alloys based on the *fcc* framework, there are reports on formation of only $L1_0$, $L1_1$, $B2$ (CsCl-type), and $\beta2$ ($MoSi_2$-type) structures to our best knowledge (Figure 3A)—indicating that researchers have not utilized all conceivable crystal structures in binary alloys. In other words, the driving forces for creating unprecedented ordered alloys remain under-investigated.

To generate such alloys, an affinity of a third element with the constituent two metal elements in binary alloys is one of driving forces for inducing an atomic rearrangement from well-known to unprecedented crystal structures. As an example [55], Goto *et al.* reported Fe−Ni−N compounds composed of an Fe−N monolayer sandwiched by two Ni monolayers when $A1$-FeNi alloys were treated with NH_3 (5 L/min) at 300 °C for 50 h. Extraction of the interstitial N atoms from Fe−Ni−N compounds under an H_2 flow (2 L/min) at 250 °C for 2 h afforded $L1_0$-FeNi ordered alloys despite the fact that complete transformation from $A1$ to $L1_0$-FeNi at <300 °C is impractical without interstitial N atoms [56]. It is hypothesized that the high affinity of N with Fe facilitates formation of $L1_0$-FeNi [57]. Considering this element affinity as inter-element miscibility—between a third metal element and the constituent two metal elements at an atomic level—in binary alloy phase diagrams [50], we formed NMs with an unprecedented crystal structure composed of an alternate $L1_0$-type PdFePd trilayer and a Pd–In ordered alloy monolayer [34]. This crystal structure is theoretically termed $Z3$-type $Fe(Pd,In^d)_3$ (Figure 3B), where the superscript refers to the **Wyckoff letter**. First-principles calculations strongly indicate

that $Z3$-type Fe(Pd,In^{d})$_3$ NMs have almost no substantial difference in the original **electron densities of states (DOS)** of the $Z3$-FePd$_3$ phase, indicative of a pseudo-binary alloy phase [58-60]. The Fe–Pd–In system is the only successful example of creating unprecedented ordered crystal structures from a large body of research on introducing a small quantity of third elements into binary alloys [61-63]. Two requirements are considered to be essential for forming the $Z3$-type crystal structure: inter-element miscibility of In, which is miscible with Pd but is immiscible with Fe; and reductive annealing of the nanoparticulate precursor powders with $A1$-PdIn$_x$@FeO$_y$ core@shell structures for quick and complete atom diffusion, as mentioned in a subsequent paragraph.

First-principles calculations also reveal the change in **formation energies** of $L1_2$-type and $Z3$-type Fe–Pd–In with increasing quantity of In (Figure 4A, B). Without addition of In, $L1_2$-FePd$_3$ is thermodynamically more favorable than $Z3$-FePd$_3$, whereas $Z3$-type Fe(Pd,In^{d})$_3$ is more stable than $L1_2$-type (Fe,In)Pd$_3$ in the range of In/(In+Pd) > 8 atomic % (at.%), where Fe(Pd,In^{d})$_3$ is most stable in the $Z3$-type structure and (Fe,In)Pd$_3$ is most stable in the $L1_2$-type structure (Figure 4A). Moreover, what will happen when substituting other metal elements M (M = Zn, Ga, Ge, Cd, Sn, Hg, Tl, and Pb) instead of In for Pd? The formation energies of $L1_2$-type and $Z3$-type Fe–Pd–M indicate that the $Z3$-type structure was more favorable only by choosing elements that are immiscible with Fe but miscible with Pd (Cd, Hg, Tl, and Pb) [50, 64], and was still unfavorable by choosing elements that are miscible with Fe and Pd (Zn, Ga, Ge, and Sn) [50] (Figure 4C). In fact, $Z3$-type Fe(Pd,Pb^{d})$_3$ NMs were formed by a similar synthetic procedure as that of $Z3$-Fe(Pd,In^{d})$_3$ NMs. These results strongly indicate that the inter-element miscibility of third elements works as a stabilizer of a thermodynamically unstable crystal structure such as the $Z3$-type structure.

*Z*3-type Fe(Pd,In^{d})$_3$ is a thermodynamically stable phase in bulk, because the aforementioned calculations were conducted for bulk and *Z*3-type Fe(Pd,In^{d})$_3$ microparticles can be experimentally formed. Our report is the first example [34] of forming a *Z*3-type Fe(Pd,In^{d})$_3$ structure despite the fact that various alloys have been synthesized by a metallurgical approach [65-67]. The bottleneck for synthesizing unprecedented alloys that include immiscible elements might be the extremely slow diffusion rate of third elements that are immiscible with one of the constituent elements [68]. Indeed, the *Z*3-type phase was not obtained by reductive annealing of the mixture of Fe–Pd nanoparticulate precursor powders with Pd@FeO$_x$ core@shell structure and In micropowders, whereas the *Z*3-type structure was formed by the same heat treatment at 800 °C for 3 h of the Fe–Pd–In nanoparticulate precursor powders with the *A*1-PdIn$_x$@FeO$_y$ core@shell structure (Figure 4D). These experiments strongly indicate that the slow diffusion of third elements can be overcome by reductive annealing of nanoparticulate precursor powders.

Literature investigations of the crystal structures of multi-component alloys by using the concept of inter-element miscibility are insufficient because of the extremely slow diffusion rate of additional elements. Reductive annealing of nanoparticulate precursor powders enables investigation of this field, resulting in formation of the unprecedented *Z*3-type Fe(Pd,In^{d})$_3$ structure induced by the inter-element miscibility of In with Fe and Pd. Thus, both inter-element miscibility and precise control over the elemental composition are important strategies for developing novel crystal structures, especially formation of various new frameworks.

Catalytic properties enhanced by novel crystal structures

Metal NMs with novel atomic arrangements exhibit different DOS from those with well-known structures and unique surfaces, which provides us with a chance for enhancing physical and chemical properties such as hydrogen-storage capacity, magnetic properties, and catalytic activity. Here, we introduce the enhanced catalytic activities of mono-metal NMs with novel crystal structures for the hydrogen evolution reaction (HER) and improving the catalytic activities of unique ordered alloy NMs for the oxygen reduction reaction (ORR).

High catalytic activity, or low overpotential in HER in alkaline media, requires strong adsorption and low dissociation energies of H_2O on catalysts in the Volmer step ($H_2O + e^- + * \rightarrow OH^- + *H$, where *H stands for the H atom binding with catalyst), which is a rate-determining step of the HER in alkaline media [69-73]. Pt NMs are outstanding HER electrocatalysts and Pt-based alloy NMs with optimized Pt DOS have been developed to afford cheaper catalysts with higher activity and stability compared with commercial Pt NMs supported on carbon (Pt/C) [17, 74, 75]. However, other mono-metal NMs with novel crystal structures can also exhibit excellent HER activity in alkaline media. Indeed, 4H-type Ru hollow nanotubes and *hcp*-type Rh NMs with short-range ordered point defects exhibited 0.5 and 0.57 fold overpotentials, respectively, compared with Pt/C at a current density of 10 mA/cm^2 [29, 32]. These Ru and Rh NMs also showed almost constant overpotentials after 10,000 potential cycles at 0.03 to –0.04 V and 0.1 to –0.1 V, respectively. In the case of 4H-type Ru hollow nanotubes, the combination of a large surface area and a large number of step/kink sites—derived from the unique shape and crystal structure—facilitates the HER activity in addition to the modulation of the DOS in Ru [32, 76, 77]. Furthermore, the high HER activity of *hcp*-type Rh NMs with short-range ordered point defects is understood by first-principles calculations; i.e., H_2O

molecules around the ordered point defects in *hcp*-type Rh NMs are strongly bound with the Rh atoms around the defects at a more-negative adsorption energy in a manner that facilitates dissociation, compared with Pt/C and Rh/C. These results indicate that the unique surface of catalysts derived from particle morphologies and novel crystal structures (ordered stacking faults and ordered points defects) can serve as excellent active sites for the HER.

Investigating highly active and durable catalysts for the ORR is also important for obtaining high-performance polymer electrolyte fuel cells [78]. Traditional approaches for enhancing ORR activity include electronic and geometrical optimization of the {111} planes of surface Pt atomic layers of Pt-based catalysts [79, 80], denoted as Pt{111}, by synthesizing metal@Pt core@shell structures; i.e., tuning the DOS by hybridizing the orbitals between the Pt shell and the metal core (ligand effect) and changing the Pt−Pt distance by the lattice mismatch at the core/shell interface (strain effect) [81-85]. Recently, Li *et al*. demonstrated that the ORR activity of Pt was substantially enhanced by an anisotropic strain effect evoked by growth of Pt on the {111} planes of the $L1_0$-type Co–Pt–*M* (*M* = none, Mn, Fe, Ni, Cu, and Zn) structure in accordance with an eigenforce model [85] (Figure 5). Density functional theory calculations of these structures were carried out to evaluate the binding energies between the strained Pt and intermediate molecules formed during reduction of O_2 into H_2O, based on displacement of the neighboring surface atoms caused by adsorption of a molecule on the unstrained Pt{111} surface [86]. This approach reveals that the strained Pt on $L1_0$-type Co–Ni–Pt NMs exhibited the best ORR activity [i.e., a mass activity (MA) of 3.1 A/mg_{Pt} and a specific activity (SA) of 9.3 mA/cm^2, corresponding to 28 and 58 fold larger, respectively, than Pt/C in 0.1 M $HClO_4$ at 0.9 V]. Moreover, although such acidic conditions are harsh to

metals (i.e., a 25% decrease in the MA of Pt/C after 5000 potential cycles between 1.0 and 1.5 V at room temperature [87]), only 16% of the MA was lost after 30,000 potential cycles between 0.6 and 1.0 V at 60 °C. This report suggests the substantial potential of ordered alloy NM catalysts for superior ORR activity and stability in acidic media. However, the $L1_0$-type structure is the only structure that affords an anisotropic strain to Pt{111} among all well-known crystal structures, which is the bottleneck for developing high-performance catalysts for the ORR. Alternatively, $Z3$-type $Fe(Pd,In^d)_3$ revealed in our previous report [34] exhibits a unique structures such as the $L1_0$-type structure. Therefore, unprecedented ordered alloy structures could be promising for imparting anisotropic strain to Pt{111} in terms of anisotropic strain and ligand effects.

Concluding Remarks

In this review, we introduced recent progress in forming mono-metal and alloy NMs with unprecedented crystal structures, and potential applications to catalysis. The prospects expected from these unique crystal structures are enhanced catalytic activities and investigating other functions—for instance, Fe-rich high-performance permanent magnets with high magnetic anisotropy energy that are superior to $R\mathrm{Fe}_{12}$-type phase (R = Sm and Nd) [88] and larger-capacity hydrogen storage materials than *fcc*-Pd with the DOS tuned by covering a metal–organic framework [89]. In fact, $Z3$-type $Fe(Pd,In^d)_3$ NMs exhibited higher magnetic anisotropy energy (−0.213 meV/atom) than $L1_2$-type $(Fe,In)Pd_3$ (−1.38 μeV/atom), resulting in larger coercivity; whereas the saturation magnetizations were almost the same [34]. Stabilization of uninvestigated crystal structures in mono-metals and alloys remains quite challenging, but researchers can enrich the library of unprecedented crystal structures by considering the following three

pioneering approaches to NM synthesis: (1) ordered stacking faults formed by the transformation from unfavorable to more-favorable structures during growth of NMs and epitaxial growth of other mono-metals or solid–solution alloys on ordered stacking faults structures, (2) ordered point defects introduced by suppressing the atomic diffusion rate, and (3) unprecedented ordered alloy structures stabilized by substituting third elements based on the inter-element miscibility. We hypothesize that these methods in the present review will facilitate investigations of unprecedented crystal structures and contribute to breakthroughs in materials science (see Outstanding Questions).

Acknowledgments

This work was supported by the Japan Science and Technology Agency (JST), CREST [Grant No. JPMJCR21B4 (T.T.)]. This study was also supported by the Japan Society for the Promotion of Science (JSPS) KAKENHI Grants-in-Aid for Scientific Research (S) [Grant No. JP19H05634 (T.T.)], Scientific Research (B) [Grant No. JP18H01953 (R.S.)], Challenging Research (Exploratory) [Grant Nos. JP19K22231 (T.T.) and JP17K19178 (R.S.)], and for a JSPS Research Fellowship [Grant No. JP18J15062 (K.M.)]. We thank Michael Scott Long, PhD, from Edanz (https://jp.edanz.com/ac) for editing a draft of this manuscript.

Disclaimer Statement

The authors declare no financial or personal interest.

References

1. Zhang, Q. *et al.* (2022) Crystal structure control of binary and ternary solid-solution alloy nanoparticles with a face-centered cubic or hexagonal close-packed phase. *J. Am. Chem. Soc.* 144, 4224–4232
2. Wu, D. *et al.* (2022) Phase control of solid-solution nanoparticles beyond the phase diagram for enhanced catalytic properties. *ACS Mater. Au* 2, 110–116
3. Hoffmann, R. (1988) Solids and Surfaces: A Chemist's View of Bonding in Extended Structures, Wiley-VCH
4. Kusada, K. *et al.* (2013) Discovery of face-centered-cubic ruthenium nanoparticles:

Facile size-controlled synthesis using the chemical reduction method. *J. Am. Chem. Soc.* 135, 5493–5496

5. Holec, D. *et al.* (2020) Surface energy of Au nanoparticles depending on their size and shape. *Nanomaterials* 10, 484
6. Qu, Y. D. *et al.* (2017) Size-dependent cohesive energy, melting temperature, and Debye temperature of spherical metallic nanoparticles. *Phys. Met. Metallogr.* 118, 528–534
7. Chmielewski, A. *et al.* (2018) Direct measurement of the surface energy of bimetallic nanoparticles: Evidence of Vegard's rulelike dependence. *Phys. Rev. Lett.* 120, 025901
8. Amara, H. *et al.* (2022) Effect of size on the surface energy of noble metal nanoparticles from analytical and numerical approaches. *Phys. Rev. B* 105, 165403
9. Kusada, K. *et al.* (2010) Hydrogen-storage properties of solid-solution alloys of immiscible neighboring elements with Pd. *J. Am. Chem. Soc.* 132, 15896–15898
10. Kusada, K. *et al.* (2019) Emergence of high ORR activity through controlling local density-of-states by alloying immiscible Au and Ir. *Chem. Sci.* 10, 652–656
11. Zhang, Q. *et al.* (2018) Selective control of fcc and hcp crystal structures in Au–Ru solid-solution alloy nanoparticles. *Nat. Commun.* 9, 510
12. Zhang, Q. *et al.* (2019) Solid-solution alloy nanoparticles of a combination of immiscible Au and Ru with a large gap of reduction potential and their enhanced oxygen evolution reaction performance. *Chem. Sci.* 10, 5133–5137
13. Kobayashi, H. *et al.* (2012) Nanosize-induced drastic drop in equilibrium hydrogen pressure for hydride formation. *J. Am. Chem. Soc.* 134, 12390−12393
14. Huang, B. *et al.* (2017) Solid-solution alloying of immiscible Ru and Cu with enhanced CO oxidation activity. *J. Am. Chem. Soc.* 139, 4643−4646
15. Vasquez, Y. *et al.* (2008) Low-temperature solution synthesis of the non-equilibrium ordered intermetallic compounds Au_3Fe, Au_3Co, and Au_3Ni as nanocrystals. *J. Am. Chem. Soc.* 130, 11866–11867
16. Sato, K. *et al.* (2020) Order–disorder transitions confined at the interface of Pd@Co core–shell nanoparticles: Implications for magnetic recording. *ACS Appl. Nano Mater.* 3, 1592−1599
17. Cao, Z. *et al.* (2017) Platinum-nickel alloy excavated nano-multipods with hexagonal close-packed structure and superior activity towards hydrogen evolution reaction. *Nat. Commun*. 8, 15131
18. Wang, J. *et al.* (2020) Crystal phase-controlled growth of PtCu and PtCo alloys on 4H Au nanoribbons for electrocatalytic ethanol oxidation reaction. *Nano Res.* 13, 1970–

1975
19. Ge, Y. *et al.* (2021) Seeded synthesis of unconventional 2H-phase Pd alloy nanomaterials for highly efficient oxygen reduction. *J. Am. Chem. Soc.* 143, 17292–17299
20. Pirart, J. *et al.* (2019) Reversed size-dependent stabilization of ordered nanophases. *Nat. Commun.* 10, 1982
21. Zhuang, J. *et al.* (2020) Phase-controlled synthesis of Ni nanocrystals with high catalytic activity in 4-nitrophenol reduction. *J. Mater. Chem. A* 8, 22143–22154
22. Wakisaka, T. *et al.* (2020) Discovery of face-centred cubic Os nanoparticles. *Chem. Commun.* 56, 372-374
23. Janssen, A. *et al.* (2022) Phase-controlled synthesis of Ru nanocrystals via template-directed growth: Surface energy versus bulk energy. *Nano Lett.* 22, 3591−3597
24. You, R. *et al.* (2022) Revealing surface restraint-induced hexagonal Pd nanocrystals via in situ transmission electron microscopy. *Nano Lett.* 22, 4333−4339
25. Huang, J. L. *et al.* (2017) Formation of hexagonal-close packed (HCP) rhodium as a size effect. *J. Am. Chem. Soc.* 139, 575−578
26. Huang, X. *et al.* (2011) Synthesis of hexagonal close-packed gold nanostructures. *Nat. Commun.* 2, 292
27. Fan, Z. *et al.* (2015) Stabilization of 4H hexagonal phase in gold nanoribbons. *Nat. Commun.* 6, 7684
28. Cheng, H. *et al.* (2021) Quasi-epitaxial growth of magnetic nanostructures on 4H-Au nanoribbons. *Adv. Mater.* 33, 2007140
29. Zhang, Z. *et al.* (2021) Evoking ordered vacancies in metallic nanostructures toward a vacated Barlow packing for high-performance hydrogen evolution. *Sci. Adv.* 7, eabd6647
30. Ge, Y. *et al.* (2020) Phase-selective epitaxial growth of heterophase nanostructures on unconventional 2H-Pd nanoparticles. *J. Am. Chem. Soc.* 142, 18971−18980
31. Tan, Z. *et al.* (2022) Slow synthesis methodology-directed immiscible octahedral Pd_xRh_{1-x} dual-atom-site catalysts for superior three-way catalytic activities over Rh. *Angew. Chem. Int. Ed.* 61, e202202588
32. Lu, Q. *et al.* (2018) Synthesis of hierarchical 4H/fcc Ru nanotubes for highly efficient hydrogen evolution in alkaline media. *Small* 14, 1801090
33. Chepulskii, R. V. *et al.* (2012) Ab initio theory of phase stability and structural selectivity in Fe-Pd alloys. *Phys. Rev. B* 85, 144201
34. Matsumoto, K. *et al.* (2022) Inter-element miscibility driven stabilization of ordered pseudo-binary alloy. *Nat. Commun.* 13, 1047

35. Chakraborty, I. *et al.* (2011) Novel hexagonal polytypes of silver: Growth, characterization and first-principles calculations. *J. Phys.: Condens. Matter.* 23, 325401
36. Jiang, R. *et al.* (2022) Non-equilibrium synthesis of stacking faults-abundant Ru nanoparticles towards electrocatalytic water splitting. *Appl. Catal. B Environ.* 316, 121682
37. Wang, C. *et al.* (2016) Creation of controllable high-density defects in Silver nanowires for enhanced catalytic property. *Nano Lett.* 16, 5669−5674
38. Trinh, T. T. *et al.* (2015) Visible to near-infrared plasmon-enhanced catalytic activity of Pd hexagonal nanoplates for the Suzuki coupling reaction. *Nanoscale* 7, 12435–12444
39. Tan, T. *et al.* (2021) Resolving the stacking fault structure of silver nanoplates. *Nanoscale* 13, 195–205
40. Huang, X. *et al.* (2012) Graphene oxide-templated synthesis of ultrathin or tadpole-shaped Au nanowires with alternating hcp and fcc domains. *Adv. Mater.* 24, 979–983
41. Lin, H. *et al*. (2020) Compensation between surface energy and hcp/fcc phase energy of late transition metals from first-principles calculations. *J. Phys. Chem. C* 124, 11005−11014
42. von Mentlen, J.-M. *et al.* (2022) Engineering of oxide protected gold nanoparticles. *J. Phys. Chem. Lett.* 13, 5824–5830
43. Fan, Z. *et al.* (2017) Epitaxial growth of unusual 4H hexagonal Ir, Rh, Os, Ru and Cu nanostructures on 4H Au nanoribbons. *Chem. Sci.* 8, 795–799
44. Fan, Z. *et al.* (2016) Synthesis of 4H/fcc noble multimetallic nanoribbons for electrocatalytic hydrogen evolution reaction. *J. Am. Chem. Soc.* 138, 1414−1419
45. Fan, F.-R. *et al.* (2008) Epitaxial growth of heterogeneous metal nanocrystals: From gold nano-octahedra to palladium and silver nanocubes. *J. Am. Chem. Soc.* 130, 6949–695
46. Tianou, H. *et al.* (2017) Inflating hollow nanocrystals through a repeated Kirkendall cavitation process. *Nat. Commun.* 8, 1261
47. Chee, S. W. *et al.* (2019) Interface-mediated Kirkendall effect and nanoscale void migration in bimetallic nanoparticles during interdiffusion. *Nat. Commun.* 10, 2831
48. Liu, N. *et al.* (2019) Point-defect distribution and transformation near the surfaces of AlGaN films grown by MOCVD. *J. Phys. Chem. C* 123, 8865−8870
49. Wakisaka, T. *et al.* (2020) Rational synthesis for a noble metal carbide. *J. Am. Chem. Soc.* 142, 1247−1253
50. Massalski, T. B. et al. (1990) Binary Alloy Phase Diagrams, ASM International

51. Cable, R. E. *et al.* (2007) Solution synthesis of nanocrystalline M-Zn (M = Pd, Au, Cu) intermetallic compounds via chemical conversion of metal nanoparticle Precursors. *Chem. Mater.* 19, 4098–4104
52. Clarysse, J. *et al.* (2021) Size- and composition-controlled intermetallic nanocrystals via amalgamation seeded growth. *Sci. Adv.* 7, eabg1934
53. Zhou, Y. *et al.* (2019) Pressure-induced irreversible evolution of superconductivity in $PdBi_2$. *Phys. Rev. B* 99, 054501
54. Sun, D. *et al.* (2019) Ordered intermetallic Pd_3Bi prepared by an electrochemically induced phase transformation for oxygen reduction electrocatalysis. *ACS Nano* 13, 10818−10825
55. Goto, S. *et al.* (2017) Synthesis of single-phase $L1_0$-FeNi magnet powder by nitrogen insertion and topotactic extraction. *Sci. Rep.* 7, 13216
56. Bordeaux, N. *et al.* (2016) Thermodynamic and kinetic parameters of the chemical order–disorder transformation in $L1_0$ FeNi (tetrataenite). *Acta Mater.* 103, 608–61
57. Wang, J. *et al.* (2022) Massive transformation in FeNi nanopowders with nanotwin-assisted nitridation. *Sci. Rep.* 12, 3679
58. Kobayashi, H. *et al.* (2015) Creation of novel solid-solution alloy nanoparticles on the basis of density-of-states engineering by interelement Fusion. *Acc. Chem. Res.* 48, 6, 1551–1559
59. Xie, W. *et al.* (2019) Theoretical design of a technetium-like alloy and its catalytic properties. *Chem. Sci.* 10, 5461–5469
60. Tsai, A. P. *et al.* (2017) Intermetallic: A pseudoelement for catalysis. *Acc. Chem. Res*. 50, 2879−2885
61. Yasuhara, A. and Sannomiya, T. (2022) Atomically localized ordered phase and segregation at grain boundaries in Au−Ag−Cu ternary alloy nanoparticles. *J. Phys. Chem. C* 126, 1160−1167
62. Nakaya, Y. *et al.* (2020) Active, selective, and durable catalyst for alkane dehydrogenation based on a well-designed trimetallic alloy. *ACS Catal.* 10, 5163−5172
63. Zhu, J. *et al.* (2018) Copper-induced formation of structurally ordered Pt−Fe−Cu ternary intermetallic electrocatalysts with tunable phase structure and improved stability. *Chem. Mater.* 30, 5987−5995
64. Kubaschewski, O. (1982) Iron—Binary Phase Diagrams, Springer
65. Kojima, T. *et al.* (2021) Screening of ternary intermetallic catalysts is possible using metallurgical synthesis: Demonstration on heusler alloys. *Kona Powder Part. J.* 38, 110–121

66. Shen, Q. *et al.* (2018) Microstructure, martensitic transformation and elastocaloric effect in Pd-In-Fe polycrystalline shape memory alloys. *Intermetallics* 100, 27–31
67. Govind, B. *et al.* (2020) Structural and magnetic properties of $Ni_{1+x}MnSb$ bulk heusler composite materials. *ACS Omega* 5, 11895−11900
68. Bernasconi, R. and Magagnin, L. (2019) Ruthenium as diffusion barrier layer in electronic interconnects: Current literature with a focus on electrochemical deposition methods. *J. Electrochem. Soc.* 166, D3219–D3225
69. Mahmood, J. *et al.* (2017) An efficient and pH-universal ruthenium-based catalyst for the hydrogen evolution reaction. *Nat. Nanotech.* 12, 441–446
70. Wang, J. *et al.* (2022) Manipulating the water dissociation electrocatalytic sites of bimetallic nickel-based alloys for highly efficient alkaline hydrogen evolution. *Angew. Chem. Int. Ed.* 61, e202202518
71. Liu, L. *et al.* (2020) Enhancing the understanding of hydrogen evolution and oxidation reactions on Pt(111) through ab initio simulation of electrode/electrolyte kinetics. *J. Am. Chem. Soc.* 142, 4985−4989
72. Wang, X. *et al.* (2020) Strategies for design of electrocatalysts for hydrogen evolution under alkaline conditions. *Mater. Today* 36, 125–138
73. Tan, H. *et al.* (2022) Engineering a local acid-like environment in alkaline medium for efficient hydrogen evolution reaction. *Nat. Commun.* 13, 2024
74. Zhang, C. *et al.* (2021) H_2 in situ inducing strategy on Pt surface segregation over low Pt doped $PtNi_5$ nanoalloy with superhigh alkaline HER activity. *Adv. Funct. Mater.* 31, 2008298
75. Alinezhad, A. *et al.* (2019) Direct growth of highly strained Pt islands on branched Ni nanoparticles for improved hydrogen evolution reaction activity. *J. Am. Chem. Soc.* 141, 16202−16207
76. Zheng, Y. *et al.* (2016) High electrocatalytic hydrogen evolution activity of an anomalous ruthenium catalyst. *J. Am. Chem. Soc.* 138, 16174−16181
77. Li, Y. *et al.* (2018) Crystallinity dependence of ruthenium nanocatalyst toward hydrogen evolution reaction. *ACS Catal.* 8, 5714−5720
78. Pollet, B. G. *et al.* (2019) Current status of automotive fuel cells for sustainable transport. *Curr. Opin. Electrochem.* 16, 90–95
79. Lopes, P. P. *et al.* (2016) Relationships between atomic level surface structure and stability/activity of platinum surface atoms in aqueous environments. *ACS Catal.* 6, 2536−2544
80. Stamenkovic, V. R. *et al.* (2007) Improved oxygen reduction activity on $Pt_3Ni(111)$ via increased surface site availability. *Science* 315, 493–497

81. Bu, L. *et al.* (2016) Biaxially strained PtPb/Pt core/shell nanoplate boosts oxygen reduction catalysis. *Science* 354, 1410–1414
82. Lopes, P. P. *et al.* (2020) Eliminating dissolution of platinum-based electrocatalysts at the atomic scale. *Nat. Mater.* 19, 1207–1214
83. Wu, Z. P. *et al.* (2021) Alloying–realloying enabled high durability for Pt–Pd-3d-transition metal nanoparticle fuel cell catalysts. *Nat. Commun*. 12, 859
84. Asano, M. *et al.* (2016) Oxygen reduction reaction activity for strain-controlled Pt-based model alloy catalysts: Surface strains and direct electronic effects induced by alloying elements. *ACS Catal.* 6, 5285−5289
85. Li, J. *et al.* (2020) Anisotropic strain tuning of $L1_0$ ternary nanoparticles for oxygen reduction. *J. Am. Chem. Soc.* 142, 19209−19216
86. Sharma, S. *et al.* (2019) Face-centered tetragonal (FCT) Fe and Co alloys of Pt as catalysts for the oxygen reduction reaction (ORR): A DFT study. *J. Chem. Phys.* 150, 041704
87. Nagasawa, K. *et al.* (2014) Performance and durability of Pt/C cathode catalysts with different kinds of carbons for polymer electrolyte fuel cells characterized by electrochemical and in situ XAFS techniques. *Phys. Chem. Chem. Phys.* 16, 10075–10087
88. Trinh, T. T. *et al.* (2021) Synthesis of mesoscopic particles of multicomponent rare earth permanent magnet compounds. *Sci. Technol. Adv. Mater.* 22, 38–54
89. Li, G. *et al.* (2014) Hydrogen storage in Pd nanocrystals covered with a metal–organic framework. *Nat. Mater.* 13, 802–806
90. Wang, Q. *et al.* (2019) Ultra-stable 4H-gold nanowires up to 800 °C in a vacuum. *J. Mater. Chem. A* 7, 23812–23817
91. Li, Q. *et al.* (2018) Pressure-induced phase engineering of gold nanostructures. *J. Am. Chem. Soc.* 140, 15783–15790
92. Han, S. *et al.* (2020) Gas-assisted transformation of gold from fcc to the metastable 4H phase. *Nat. Commun.* 11, 552 (2020)
93. Matsumoto, K. *et al.* (2019) Formation of strong $L1_0$-FePd/α-Fe nanocomposite magnets by visualizing efficient exchange coupling. *Nanoscale Adv.* 1, 2598–2605.
94. Lei, W. *et al.* (2019) Cu induced low temperature ordering of fct-FePtCu nanoparticles prepared by solution phase synthesis. *J. Mater. Chem. C* 7, 11632–11638

Table 1. Summary of experimentally formed unprecedented crystal structures

Crystal structure	Materials	Approaches	References
4H	Au	Growth from 2H-Au nanowire	[27]
		Dealloying of *A*3-Au–Ga	[42]
	Ag, Rh, Os, Ru, Cu, Pt−Cu, Pt−Co, Ag−Pd, Pt−Ag, and Pt−Pd−Ag	Epitaxial growth of metals on 4H-Au nanoribbons	[18, 32, 43, 44]
14H	Co	Epitaxial growth of metals on 4H-Au nanoribbons	[28]
hcp-type phase with short-range ordered point defects	Rh	Atomic diffusion rate suppressed by unique morphology	[29]
*Z*3-type phase	$Fe(Pd,In^{d})_3$ and $Fe(Pd,Pb^{d})_3$	Additional third element based on inter-element miscibility	[34]

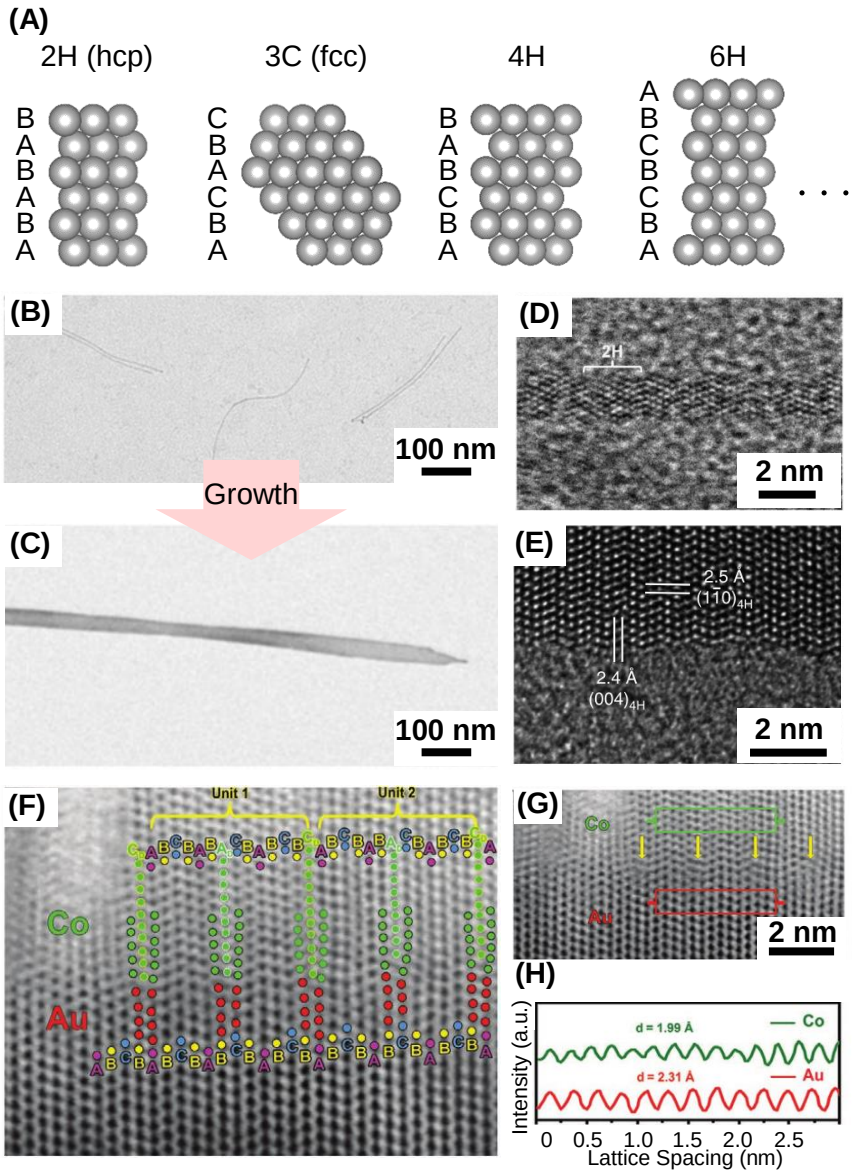

Figure 1. Mono-metal nanomaterials with ordered stacking faults. (A) Variation of ordered stacking faults; where C is cubic, H is hexagonal, and the numerical characters are repeating numbers of a close-packed plane. (B–E) Transmission electron microscopy (TEM) and high resolution TEM (HRTEM) images of Au nanowires (B and D) and nanoribbons (C and E). (F–H) HRTEM images of 4H-type Au and 14H-type Co phases (F and G) as well as the integrated pixel intensities in G (H). Reproduced from (B–E) ref.

27 and with permission from (F–H) ref. 28. Copyright 2021, John Wiley and Sons.

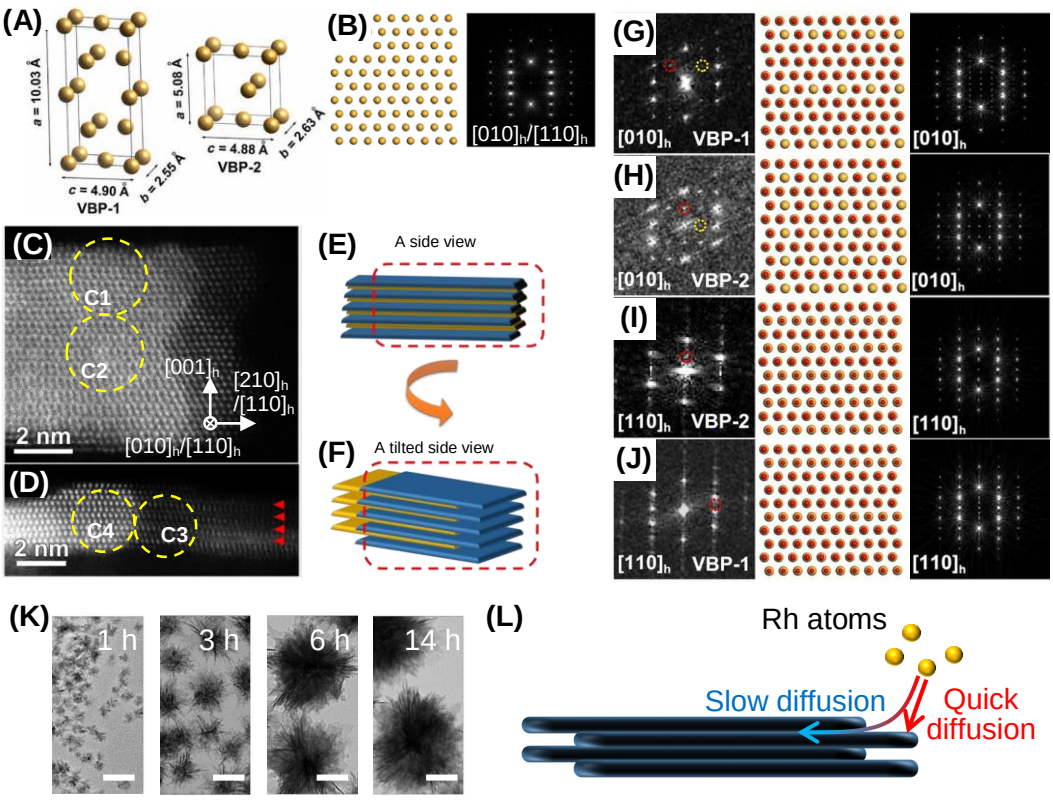

Figure 2. Formation of *hcp*-type Rh with short-range ordered point defects. (A) Model of the unit cells for two-type vacated Barlow packing (VBP-1 and VBP-2) of *hcp*-type Rh; where Barlow packing is a general term for e.g. 2H, 3C, 4H, and 6H. (B) Model of *hcp*-Rh structure without ordered point defects from $[010]_h$ or $[110]_h$ and its fast Fourier-transform (FFT) image. (C–F) High-angle annular dark-field scanning transmission electron microscopy (HAADF–STEM) images (C and D) observed from two angles (E and F, respectively). (G–J) FFT images (left images) obtained from C1–C4 in the HAADF–STEM images (C and D), respectively, and the VBP (middle) and FFT (right) images corresponding to the experimental FFT images (left images). (K) Transmission electron microscopy images of Rh NMs synthesized by time-dependent experiments. (Scale bar: 50 nm) (L) Schematic of atomic diffusion rate limited by atomic-level

intercalated Rh nanosheets. Reproduced from (A–K) ref. 29.

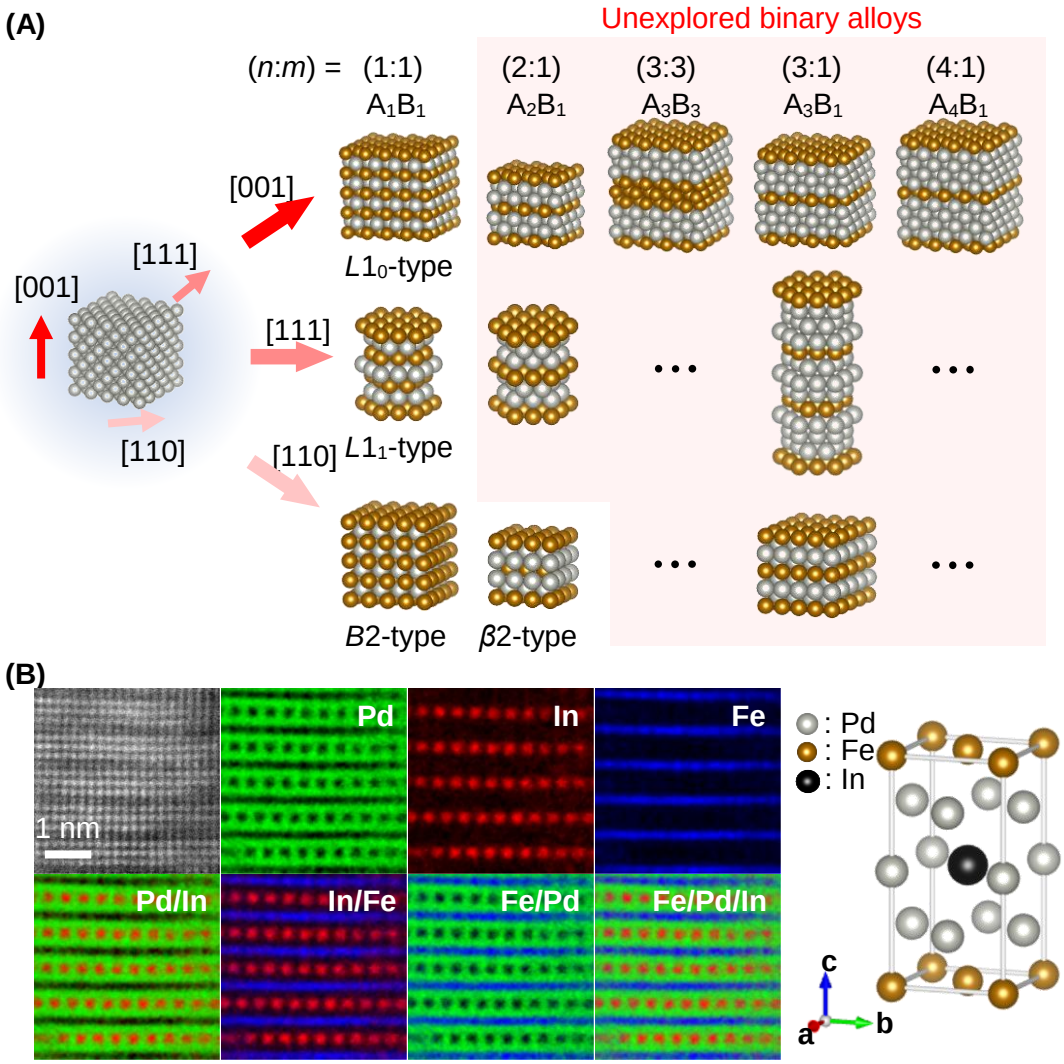

Figure 3. First synthesis of pseudo-*Z*3 structure in uninvestigated binary alloys. (A) Various ordered binary alloys based on the *fcc* framework. (B) High-angle annular dark-field scanning transmission electron microscopy and atomic-resolution energy-dispersive X-ray spectroscopy images, and the model of the unit cell in *Z*3-type $Fe(Pd,In^{d})_3$, where the superscript refers to the Wyckoff letter. Reproduced from ref. 34.

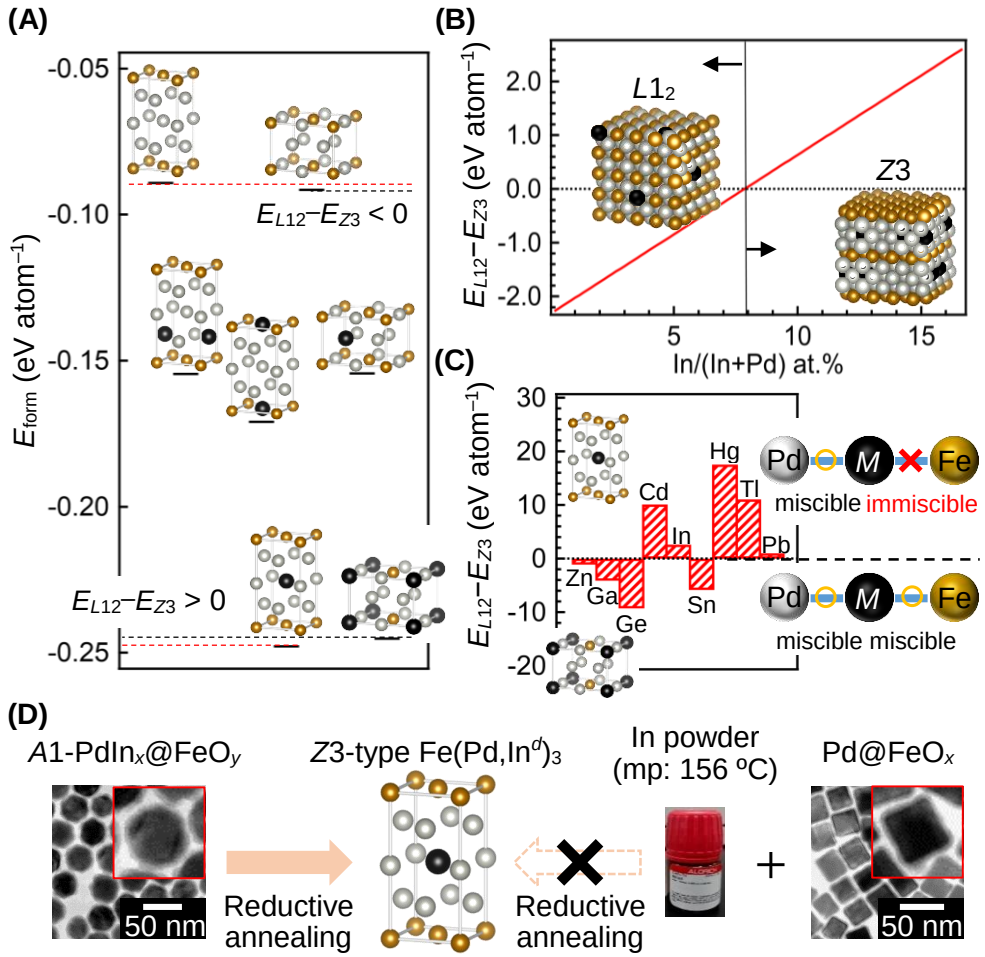

Figure 4. Key factors for forming the *Z*3-type Fe(Pd,In^d)$_3$ structure. (A) Formation energies (E_{form}) of *Z*3-type and $L1_2$-type $Fe_aPd_bIn_c$ [(*a*, *b*, *c*) = (2, 6, 0), (1, 6, 1), and (2, 5, 1)] obtained from first-principles calculations, corresponding to $E[L1_2$- or *Z*3-type $Fe_aPd_bIn_c] - (aE[Fe] + bE[Pd] + cE[In])$, where $E[X]$ is equivalent to the total energies of *X* at the ground states. (B) Change of E_{L12} and E_{Z3} dependent on the quantity of In, where E_{L12} and E_{Z3} are equal to $x\times E[L1_2\text{-}(Fe_1, In_1)Pd_6] + (1–x) \times E[L1_2\text{-}Fe_2Pd_6] + x\times E[Fe]$ and $x\times E[Z3\text{-}Fe_2(Pd_5, In_1{}^d)] + (1–x) \times E[Z3\text{-}Fe_2Pd_6] + x\times E[Pd]$ ($0 \le x \le 1$), respectively. (C) Difference of E_{L12} and E_{Z3} ($x = 1$) in the case of substituting *M* instead of In (*M* = Zn, Ga, Ge, Cd, Sn, Hg, Tl, and Pb). (D) Schematic indicating that nanoscale-homogeneous

nanoparticulate precursor powder is a key factor for forming *Z*3-type $Fe(Pd,In^{d})_3$. Reproduced from ref. 34.

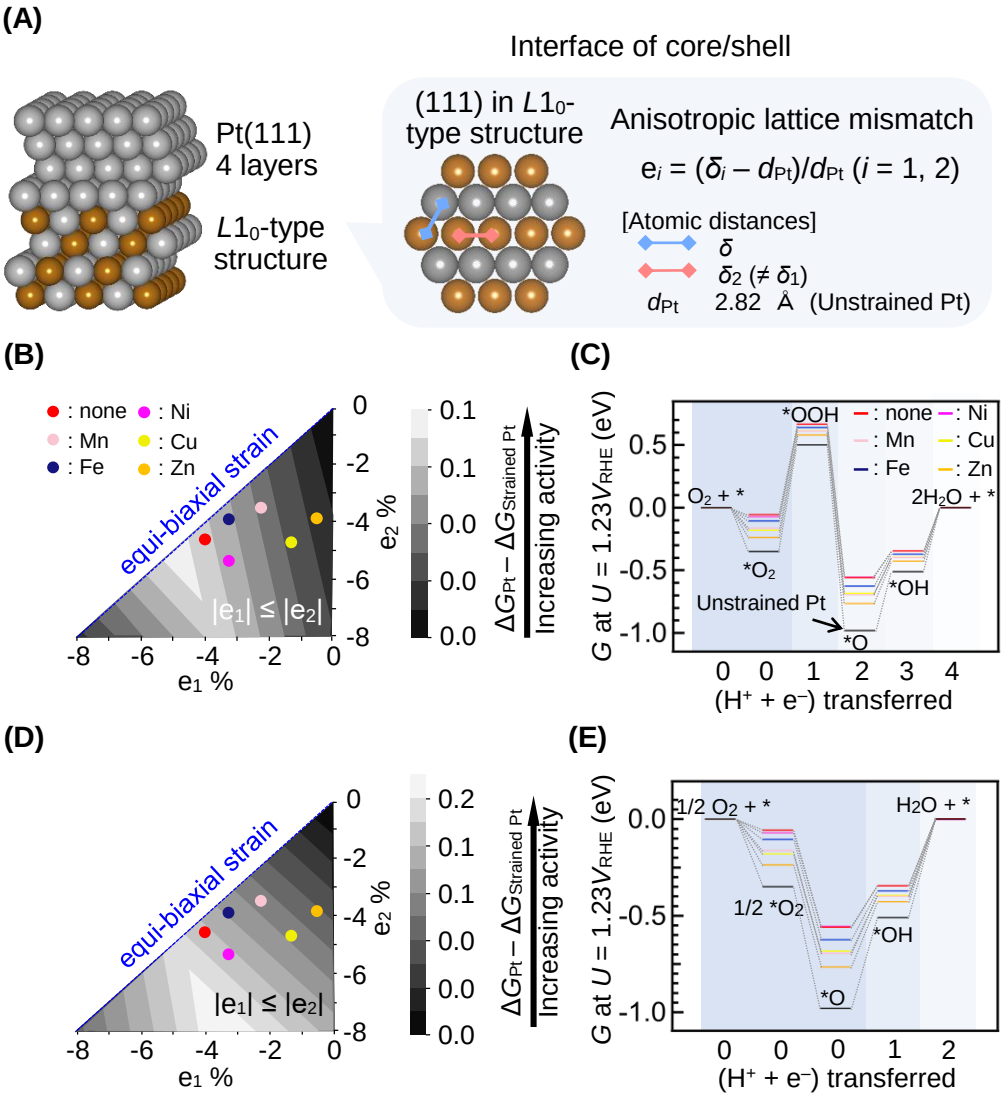

Figure 5. Oxygen reduction reaction (ORR) activity of Pt enhanced by anisotropic strain. (A) Model of $L1_0$-alloy@$Pt_{4\text{-layer}}$ core@shell structure and anisotropic lattice mismatch introduced on the {111} planes of the Pt shell (Pt{111}) induced by the {111} planes of the $L1_0$-type structure. (B and D) Strain–ORR activity relationship for associative (B) and dissociative (D) mechanisms, where $G_{Pt} - \Delta G_{Strained\ Pt}$ corresponds to the difference in these activation barriers at the reactions [$*O_2 + H^+ + e^- \rightarrow *OOH$ (B) and $*OH + H^+ + e^- \rightarrow H_2O + *$ (C), where * refers to the state of adsorption on the catalysts]. (C and E) Gibbs

free energies for the ORR on unstrained and strained Pt via associative (C) and dissociative (E) mechanisms. Reproduced with permission from (B–E) ref. 85. Copyright 2020, American Chemical Society.

Keywords

Nanomaterials, ordered stacking fault, ordered point defect, inter-element miscibility, ordered alloy

Glossary

Bulk energy: internal energy when the total energy of a substance is divided into internal and surface energies

Cohesive energy: energy required to separate each atom from a solid

Density of states (DOS): electron energy distribution formed by orbital hybridizations between all of the atoms in a solid. The shape of the DOS is determined by the symmetry of the structure, the inter-atom distance, and the species of the constituent elements. In particular, the DOS for electrons with a maximum energy near the Fermi level is used to describe various physical and chemical properties, such as electrical conductivity and catalytic properties.

First-principles calculations: method of solving the kinetic energy of electrons in a substance by numerical calculations in accordance with quantum theory. In many cases, an approximate solution is obtained by expressing the electrons in terms of their density; i.e., by using density functional theory.

Formation energy: difference in energy between the bulk energy of the alloy and the bulk energy of each constituent element; i.e., the energy obtained by alloying

Intermetallic binary alloy: alloy structure in which the constituent elements in a binary alloy are arranged at specific atomic positions

Kirkendall effect: phenomenon in which hollows are formed in a substance because of differences in the rate of atomic diffusion for each element in the substance. This cavity formation indicates that atoms diffuse by using defects in the material.

Solid–solution alloy: alloy structure in which multiple elements are randomly arranged based on the crystal structure of a mono-metal

Wyckoff letter: nonequivalent atomic positions in the unit cell based on the space group. In addition, atomic positions are often expressed by adding the multiplicity of equivalent atomic positions. In the case of *Z*3-type $Fe(Pd,In^{d})_3$, the space group is *P*4/*mmm* and the atomic positions are Fe^{1a} (0, 0, 0), Fe^{1c} (0.5, 0.5, 0), Pd^{4i} (0.5, 0, 0.23), Pd^{1b} (0, 0, 0.5), and In^{1d} (0.5, 0.5, 0.5).

Highlights

An investigation of unprecedented crystal structures enables development of new functions and enhancement of well-known properties.

Although an infinite number of crystal structures are geometrically possible, the crystal structures of metal nanoparticles depend on thermodynamics.

Mono-metal nanoparticles with ordered stacking faults and ordered point defects, as well as unprecedented ordered alloy nanoparticles, are generated by stabilization.

Stabilization is by (1) transformation from unfavorable to more-favorable structures during growth of the nanoparticles and epitaxial growth of other metals on ordered stacking faults structures, (2) suppression of the atomic diffusion rate, and (3) substitution of third elements based on the inter-element miscibility.

Box 1. Formation of metastable alloy NMs with well-known crystal structures

Metastable alloy NMs with well-known crystal structures stabilized by nano-size effect have been synthesized by kinetic chemical synthesis methods. For example, solid-solution alloys between immiscible elements have been obtained by a simultaneous reduction of multiple metal precursors with different redox potentials [1, 2, 9-15]. Moreover, control over the crystal structure can be also done by fine-tuning of the reduction rate in the simultaneous reduction procedure [1]. Interestingly, the kinetically formed metastable alloy NMs can potentially transform into different metastable phases by an appropriate external stimulus. For example, Pd–Ru alloy composed of immiscible elements transformed from *A*1 to *A*3 structures by introducing hydrogen atoms [2]. Therefore, the modification of nucleation process is important for the alloying of immiscible elements and the formation of metastable crystal structures.

Box 2. Phase stability of Au nanoribbons with 4H structure

4H-Au nanoribbons, which are used as templates for forming 4H structures of various mono-metals and solid solution alloys, are stable under high temperature and high pressure. According to in situ TEM observation under high temperature, 4H structure was kept until < 800 °C [90]. As a result of the pressurization experiment at room temperature, it was confirmed that the 4H structure was maintained up to 1.2 GPa and the 4H structure was maintained as an *fcc*/4H heterostructure up to about 26 GPa [91]. Surprisingly, in situ TEM under 1 mbar of CO gas observed the transformation of *fcc* (stable phase) to 4H (metastable phase) structures of Au nanospheres on 4H-Au nanoribbons [92]. First-principles calculations and experiments strongly support that this phase transition is driven by surface energy gain that exceeds bulk energy loss. These results indicate that 4H-Au nanoribbon is an effective material as a template for the 4H phase formation of other metals.

Box 3. Formation of intermetallic compound NMs

A large difference in redox potentials is a serious problem in synthesizing intermetallic compound NMs, because the simultaneous reduction method tends to form a phase-segregated structure. Then, a step-by-step chemical synthesis method is effective for alloying such an element pair. For example, after the growth of metal oxides (low redox potential) on noble metal NMs (high redox potential) with monodisperse size and shape, the reductive annealing for the nanoparticulate precursor powders is conducted at high temperature (>500 °C), by which highly ordered intermetallic compound NMs are formed [34, 93]. Recently, in order to avoid the inter-particle fusion happening at such a high

temperature, the synthesis of intermetallic compounds NMs by the introduction of a third element [94] and alloying noble metal NMs with base metals in a solution that excludes oxygen [51, 52] have been reported. In both methods, relatively high temperature around 300 °C in a solution system allows the atomic diffusion within particles and the formation of intermetallic compounds. These approaches facilitate the control of particle size and shape, and the investigation on the phase stability of intermetallic compounds including or excluding nano-size effects, respectively.

Outstanding Questions

Various metastable phases have been discovered in the nanoscale regime. These phases are metastable or kinetically stable in bulk. Can we regard them to be thermodynamically stable, considering nano-size effects?

4H-Au nanoribbons are formed from 2H-Au nanowires. Is it possible to form 4H-Au nanoplates from 2H-Au nanosheets? Because 4H-Au nanoplates exhibit different surfaces compared with 4H-Au nanoribbons, can the different metastable phases be stabilized by epitaxial growth of other mono-metals or solid–solution alloys on 4H-Au nanoplates?

To reveal the contribution of C atoms in *hcp*-type Rh nanoparticles with short-range ordered point defects to the phase stability, is it possible to remove only the C atoms yet maintain the crystal structure?

Inter-element miscibility of In, which is miscible with Pd but immiscible with Fe, restricts substitution sites of In in $L1_2$ and $Z3$-$FePd_3$ structures to sites where Fe and In are not adjacent. Does such an inter-element miscibility restrict diffusion paths until forming Fe–Pd–In alloy phases? Can the $Z3$-type $Fe(Pd,In^d)_3$ structure be formed for nanoparticles smaller than 10 nm by the nano-size effect?